Blade Displacement Predictions for the Full-Scale UH-60A Airloads Rotor

Robert T. Biedron
Senior Research Scientist

Elizabeth M. Lee-Rausch
Research Engineer

NASA Langley Research Center, Hampton, VA 23681

ABSTRACT

An unsteady Reynolds-Averaged Navier-Stokes solver for unstructured grids is loosely coupled to a rotorcraft comprehensive code and used to simulate two different test conditions from a wind-tunnel test of a full-scale UH-60A rotor. Performance data and sectional airloads from the simulation are compared with corresponding tunnel data to assess the level of fidelity of the aerodynamic aspects of the simulation. The focus then turns to a comparison of the blade displacements, both rigid (blade root) and elastic. Comparisons of computed root motions are made with data from three independent measurement systems. Finally, comparisons are made between computed elastic bending and elastic twist, and the corresponding measurements obtained from a photogrammetry system. Overall the correlation between computed and measured displacements was good, especially for the root pitch and lag motions and the elastic bending deformation. The correlation of root lead-lag motion and elastic twist deformation was less favorable.

NOTATION

$()_{tip}$	denotes blade tip
$()_\infty$	denotes freestream condition
a	speed of sound [ft/s]
BD	Blade Displacement measurement system
c	section blade chord [ft]
C_{Mx}	hub rolling moment coefficient $(\frac{Mx}{\rho_\infty {V_{tip}}^2 \pi R^3})$
C_{My}	hub pitching moment coefficient $(\frac{My}{\rho_\infty {V_{tip}}^2 \pi R^3})$
C_P	rotor power coefficient $(\frac{P}{\rho_\infty {V_{tip}}^2 \pi R^2})$
C_T	rotor thrust coefficient $(\frac{T}{\rho_\infty {V_{tip}}^2 \pi R^2})$
C_X	rotor propulsive force coefficient $(\frac{X}{\rho_\infty {V_{tip}}^2 \pi R^2})$
CFD	Computational Fluid Dynamics
CSD	Computational Structural Dynamics
f_n	sectional normal force [lbf/ft]
f_c	sectional chord force [lbf/ft]
m	$c/4$ sectional pitching moment [ft-lbf/ft]
M^2C_c	sectional chord force coefficient $(\frac{f_c}{\frac{1}{2}\rho_\infty {a_\infty}^2 c})$
M^2C_m	$c/4$ sectional pitching moment coefficient $(\frac{m}{\frac{1}{2}\rho_\infty {a_\infty}^2 c^2})$
M^2C_n	sectional normal force coefficient $(\frac{f_n}{\frac{1}{2}\rho_\infty {a_\infty}^2 c})$
M_x	rotor hub rolling moment [ft-lbf]
M_y	rotor hub pitching moment [ft-lbf]
P	rotor power [ft-lbf/s]
r	radial position [ft]
R	rotor radius [ft]
T	rotor thrust [lbf]
V	velocity [ft/s]
x	chordwise distance from leading edge [ft]
X	rotor propulsive force [lbf]
α_c	corrected shaft angle [°]
α_s	geometric shaft angle [°]
μ	advance ratio $(\frac{V_\infty}{V_{tip}})$
ρ_∞	freestream density [slugs/ft^3]
σ	solidity
θ_c	collective pitch (mean root pitch) [°]
θ_{1s}	sine component of root pitch variation with azimuth [°]
θ_{1c}	cosine component of root pitch variation with azimuth [°]
ψ	azimuthal position [°]

Presented at the AHS 70th Annual Forum, Montreal, Quebec, May 20–22, 2014.

INTRODUCTION

The flight test of the UH-60A airloads rotor in 1993 provided an extensive database for the validation of predictive analysis tools. (Refs. 1, 2) Numerous studies have been published that compare loosely-coupled Computational Fluid Dynamics (CFD) and Computational Structural Dynamics (CSD) predictions with the flight test data. The use of CFD has typically shown improved comparison of airloads between flight test and computation over the lower-fidelity models available in CSD comprehensive codes. Despite a high level

of fidelity in aerodynamic modeling (including Reynolds-Averaged Navier-Stokes (RANS) and Detached-Eddy Simulations (DES)) and a high level of spatial/temporal resolution, the correlation of the predicted and measured sectional airloads has appeared to reach a plateau. (Refs. 3–5) Differences in sectional airloads between the various simulations are generally smaller than the difference between the simulations and measured data. A full-scale wind-tunnel test of the same UH-60A rotor used in the 1993 tests was completed in 2010 at the National Full-Scale Aerodynamic Complex (NFAC) 40- by 80-foot Wind Tunnel. (Ref. 6) The wind-tunnel test provided an opportunity to test the airloads rotor in a more controlled environment without the influence of a tail rotor or propulsion system. Also, the wind-tunnel test produced additional data not available from the flight test including new measurements and additional flow conditions. The new measurements include rotor balance forces and moments, oscillatory hub loads, blade displacements and deformations and rotor wake measurements. An increased confidence in both simulation and measurement can be gained through detailed comparisons of this hierarchy of data. Since the completion of the NFAC tests numerical simulations at representative conditions from the test database have begun. Initial simulations focused on comparisons with sectional airloads and rotor performance predictions. (Refs. 7,8) Computations of vortex evolution have been made using high-resolution structured grids, and compared with vortex positions derived from PIV measurements. (Ref. 9) More recently, computational results focusing on blade displacements have been made using OVERFLOW coupled to CAMRAD-II. (Refs. 10, 11)

An unsteady RANS solver for unstructured grids, FUN3D, has been used to compute the rotor performance and airloads of the UH-60A Airloads Rotor in the NFAC. (Ref. 12) The flow solver was loosely coupled to a rotorcraft comprehensive code, CAMRAD-II, to account for trim and aeroelastic deflections. Computations were made for the 1-g level flight speed-sweep test conditions with the airloads rotor installed on the NFAC Large Rotor Test Apparatus (LRTA) and in the 40- by 80-ft wind tunnel to determine the influence of the test stand and wind-tunnel walls on the rotor performance and airloads. Detailed comparisons were made between the results of the CFD/CSD simulations and the wind tunnel measurements including rotor loads, sectional loads and blade pressures. The computed trends in solidity-weighted propulsive force and power coefficient matched the experimental trends over the range of advance ratios and were comparable to previously published results. (Refs. 7, 8, 10, 13–15) Rotor performance and sectional airloads showed little sensitivity to the modeling of the wind-tunnel walls, which indicated that the rotor shaft-angle correction adequately compensated for the wall influence up to an advance ratio of 0.37. Sensitivity of the rotor performance and sectional airloads to the modeling of the rotor with the LRTA body/hub increased with advance ratio. The inclusion of the LRTA in the simulation slightly improved the comparison of rotor propulsive force between the computation and wind tunnel data at an advance ratio of 0.30, but did not resolve the difference in the rotor power predictions at an advance ratio of 0.37. Despite a more precise knowledge of the rotor trim loads and flight condition, the level of comparison between the computed and measured sectional airloads/pressures did not significantly improve over the previously published results for the flight test. (Refs. 3, 16)

The focus of the current paper is to provide detailed comparisons between blade displacements and deflections obtained from FUN3D/CAMRAD-II simulations and wind tunnel blade displacement measurements from the NFAC test. While the emphasis is on blade displacements and deflections, comparisons with overall rotor performance measurements (thrust, power and propulsive force) and sectional airload measurements (normal force, chord force and pitching moment) are also presented to provide a more complete assessment of the fidelity of the numerical simulations for the conditions considered in the current paper.

UH-60A AIRLOADS WIND TUNNEL TEST

In 2010, a full-scale wind-tunnel test of the UH-60A airloads rotor was conducted at the NFAC 40- by 80-foot Wind Tunnel. Reference 6 gives a detailed description of the test hardware, instrumentation, and data reduction. Figure 1 shows the airloads rotor mounted on the LRTA in the NFAC. The primary objective of the test was to acquire a comprehensive set of validation-quality measurements on a full-scale rotor at challenging conditions outside the conventional flight envelope. A secondary objective of the test was to provide data to evaluate the similarities and differences between small-scale wind tunnel, full-scale wind tunnel, and full-scale flight test. To meet these objectives, the test was separated into six phases: (1) 1-g level flight speed sweeps, (2) parametric sweeps, (3) airloads flight test simulations, (4) small-scale wind tunnel test simulations, (5) high advance ratio (slowed rotor) testing, and (6) particle image velocimetry (PIV) testing.

Fig. 1. UH-60A Airloads Rotor mounted on the LRTA in the NFAC 40- by 80-foot Wind Tunnel.

One blade of the airloads rotor was instrumented with 241 unsteady pressure transducers. Transducers were generally

grouped chordwise along nine radial stations. Figure 2 shows the radial stations at which test data were collected. A maximum of 15 transducers were installed on the upper-surface at each radial station, along with a maximum of 15 transducers on the lower-surface at each station. As in the flight-test program, the blade pressures were integrated to provide normal force, pitching moment, and chord force for each radial station. Although the transducers were clustered near the leading edge to better resolve the pressure distribution there, the number of points used to integrate the measured data were sparse in comparison with the number of points typically used for integration of CFD data. Furthermore, not all transducers remained operational for all of the run conditions of the test program. Aerodynamic shear stresses were not measured, so the experimental integrated sectional airloads reflect only the pressure contribution.

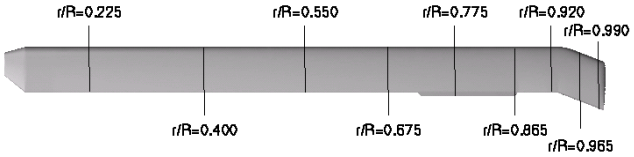

Fig. 2. UH-60A Airloads Rotor pressure transducer radial locations.

To provide an expanded database for predictive tools, an extensive set of measurements were made during the test. In addition to the blade instrumented with unsteady pressure transducers, a second blade was instrumented with strain gages. The wind-tunnel test also produced a tremendous amount of additional data not available from the flight test including rotor hub forces and moments, oscillatory hub loads, blade displacements and deformations, and rotor wake measurements. The new measurements allow for a more precise knowledge of rotor flight and trim conditions.

The blade displacement (BD) data was obtained from multi-camera photogrammetry. (Refs. 10, 17) The photogrammetry measurements were based on 48 targets distributed on the lower surface of each blade, from radial station $r/R = 0.2$ to station $r/R = 0.97$ at approximately $0.05r/R$ increments. Additional fixed targets in the tunnel ceiling were used for calibration purposes. Figure 3 shows the photogrammetry targets on the model as installed in the NFAC.

During data acquisition, three-dimensional target locations are projected onto a two-dimensional image plane. Three-dimensional target centroid coordinates are then reconstructed from multiple two-dimensional images taken from different camera positions. Coordinate transforms map the target centroids from test section coordinates to model coordinates. Comparisons with target centroid locations measured on an unloaded, undeformed blade then results in estimates of rigid and elastic deformations in pitch, flap, and lead-lag (herein referred to simply as "lag"). It should be noted that estimates of the rigid pitch, flap and lag displacements rely on a data fit of the inboard 25 % target locations, along with the assumption that the blade is effectively rigid at these inboard stations.

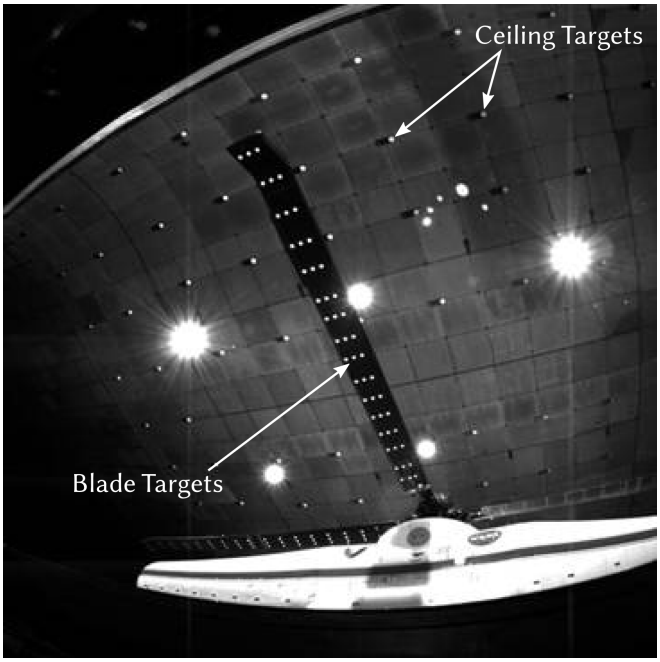

Fig. 3. Lower surface of blade with photogrammetry targets used by the Blade Displacement system.

Elastic deformations that may actually be present at these inboard stations may lead to errors in the estimates of the rigid pitch, flap and lag angles, which in turn can propagate into the estimates of the elastic deformations at other target locations. Variations in the measurements from rev-to-rev were noted and are included in the data set as standard deviations from average values over many revolutions. In general these rev-to-rev variations are small compared to blade-to-blade differences. As the data reduction for the blade deflections is quite complex, the process is still under refinement and the blade deflection data used for comparison with the computational results should be considered preliminary.

Blade displacement data from the NFAC tests are categorized as primary or secondary. Primary displacement data tracks each blade through all four quadrants of rotation. Secondary data tracks a different blade in each quadrant. Because each blade is different, piecing secondary data together to form a complete revolution will result in discontinuities at quadrant boundaries. Thus, primary data sets are preferred for comparisons with computation. Fortunately, primary data sets are available from each of the six test phases mentioned earlier.

Two alternate systems, a crab-arm system and a laser system, also provide independent measurements of the blade-root motion. The crab-arm system, which was also employed during the earlier flight-test program, uses a set of three rotary variable differential transformers (RVDTs) for each blade. The relative motions of the RVDTs are used to obtain blade-root motions by solution of three kinematic equations. The laser system was comprised of a set of three laser distance transducers, one set of three for each blade. Both crab-arm and laser data have recently been corrected to account for

transducer and amplifier drift as well as rotational (centrifugal force) effects; it is this corrected data that is compared to the computational results.

CFD/CSD METHODOLOGY

The unstructured-grid Computational Fluid Dynamics (CFD) solver used for this study is FUN3D. (Ref. 18) The code solves the unsteady RANS equations, with several models available for turbulence closure. The solver has a variety of mesh-motion options, including rigid, deforming, and overset meshes, and a robust implicit time-advancement scheme. For overset meshes, the DiRTlib (Ref. 19) and SUGGAR++ (Ref. 20) codes are used to facilitate communication between disparate zones in the mesh. For rotorcraft simulations, structural dynamics and trim are modeled by coupling with a rotorcraft comprehensive code, a specialized form of Computational Structural Dynamics (CSD) code.

In this paper, an isolated rotor in free air is modeled. An unstructured mesh with prismatic elements in the boundary layers near blade surfaces, and tetrahedra elsewhere is used to discretize the fluid volume surrounding the rotor. The blade surface geometry used for grid generation is based on an updated definition provided by the Sikorsky Aircraft Corporation via the UH-60 Airloads Workshop in May 2009. The updated geometry includes more spanwise resolution at the tip cap and a correction to the spanwise location of the trim tab. The near-body blade grid extends away from the blade to a cylindrical outer boundary of radius $1.5c_{tip}$. In the wall normal direction, the grid spacing is set such that an average normalized coordinate y^+ is less than one for the first grid cell at the wall for the majority of the blade. The maximum spacing at the blade grid outer boundary is approximately $0.10c_{tip}$. Each blade grid contains approximately 2.65 million nodes. Four blade grids are overset onto a tetrahedral background grid to form the computational grid system.

The background grid is defined in a square box whose sides extend $5R$ out from the rotor hub. The finest spacing in the off-body grid is approximately $0.10c_{tip}$. This minimum spacing is maintained, within the constraints of the unstructured meshing software, in a cylindrical volume which extends $1.1R$ in the blade plane and $0.20R$ above and $0.20R$ below the blade plane. This cylindrical volume of refinement was achieved by using volume sources. The background component grid has approximately 7.0 million nodes. The baseline composite grid has a total of approximately 17.6 million nodes. A slice through the baseline isolated UH-60 composite grid in Fig. 4 shows the spacing characteristics of the blade and off-body grids through the computational domain. The grids are shown in a vertical plane passing through the rotor hub location. The same grid system was used for simulations of an isolated UH-60A rotor system in References 3, 12, 16.

For the results presented here, the one-equation Spalart-Allmaras turbulence model is used. (Ref. 21) The turbulence model is applied to both the near-body and off-body regions. Inviscid fluxes are evaluated with a second-order (in space)

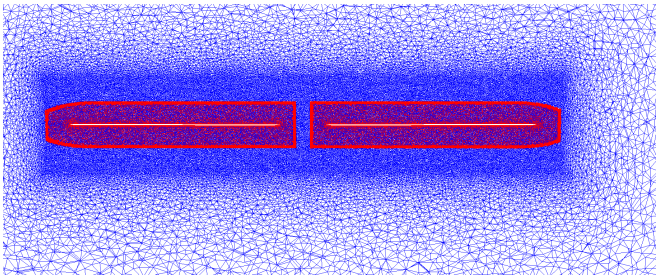

Fig. 4. Slice through the CFD grid used to model the rotor.

implementation of Roe's scheme. (Ref. 22) Time advancement is carried out with a modified second-order backward-difference dual-time scheme which results in reduced leading-order truncation error compared to the classical second-order backward-difference scheme. (Refs. 23, 24) A time step corresponding to a 1° change in blade azimuth per step is used. Time advancement is performed under the guidance of a 'temporal error controller' (Refs. 23, 25) in which dual-time subiterations are carried out within each time step until either the L_2 norm of the nonlinear residual is reduced to a specified fraction of the estimated temporal error, or, a specified maximum number of subiterations have been performed. For the current results, the error fraction is 0.05, and the maximum number of subiterations allowed is 40. In Reference 3 a detailed study of the sensitivity of FUN3D results to parameters such as grid density, turbulence model, and time step was carried out for several of the UH-60A flight-test conditions was carried out, and the results of that study were used as guidelines for the current simulations.

The rotorcraft comprehensive code used for this study is CAMRAD-II. (Ref. 26) The aerodynamics modules within CAMRAD-II are based on lifting-line models using airfoil tables, coupled with wake models. Although such aerodynamic models can provide reasonable results for many flight conditions, in some cases the predictions of the airloads can be inaccurate because of limitations of the relatively low-order aerodynamic modeling. To help overcome these limitations, loose coupling to a CFD code may be employed. In the loose coupling approach, airloads data from the CFD solver and blade motion data from the CSD solver are exchanged at relatively infrequent periodic intervals, for example once per revolution or more generally once per integer multiple of the blade passage frequency. In a typical coupled simulation, the initial execution of the FUN3D CFD code is carried out for two complete rotor revolutions, using blade deformations from a trimmed CAMRAD II solution with unmodified lifting-line aerodynamics. In subsequent coupling cycles, FUN3D is run for two blade passages between coupling cycles (i.e., one-half revolution for a four-bladed rotor such as the UH-60A). Although coupling could be performed as frequently as each blade passage, running the solver for the extra blade passage helps damp out transients between coupling cycles. When converged, the loose coupling approach replaces the low-order lifting-line aerodynamics of the CSD code with the higher-fidelity Navier-Stokes aerodynamics of the CFD

code. Loose coupling is appropriate for unsteady problems of a periodic nature, such as a rotor fixed within a wind tunnel or in steady level flight. A full description of the CFD method and coupling strategy can be found in Reference 3.

Within CAMRAD-II, each blade is modeled as a set of nonlinear beam elements. In addition to the structural dynamics modeling, CAMRAD-II offers a sophisticated trim capability. For the UH-60A wind-tunnel test conditions presented here, a three-degree-of-freedom trim is used, with the (solidity-weighted) thrust coefficient, pitching moment and rolling moment specified as trim targets within CAMRAD-II. The same, widely used CAMRAD-II structural dynamics model established in Reference 27 was employed in this study, with a couple of modifications that were also used in References 11, 12. The first change was to increase the number of radial aerodynamic panels from 20 to 100. The second change was to increase the azimuthal resolution within CAMRAD-II from 24 to 360 steps per revolution. As in the standard model, seven one-dimensional structural beam elements were used to model the rotor blade.

RESULTS

During the NFAC tests, data were acquired during all six phases of the test campaign to obtain blade displacements and deflections with the BD system. Of these, two cases classified as primary BD points were numerically simulated and are presented in this paper. Run 43 Points 60-63 (herein referred to as R43P60) represents a moderate thrust, moderate advance ratio condition. This run was part of a parametric sweep during which the fixed-system hub moments were nominally zero. Run 53 Points 20-25 (R53P20) represents a low thrust, high advance ratio condition, and was part of the 1-g level flight test phase designed to cover representative flight conditions of the UH-60A, including representative hub moments. As in any test situation, conditions varied slightly from test point to test point. Average test conditions for these two data sets are summarized in Table 1. These test points have also been examined using OVERFLOW/CAMRAD-II: R42P60 in Reference 10 and R53P20 in Reference 11.

Run/Pt	$\alpha_c(deg)$	μ	M_{tip}	C_T/σ	M_X, M_Y (ft-lb)
R42P60	0.78	0.300	0.649	0.1002	$-50\ M_Y$
					$44\ M_X$
R53P20	-7.99	0.371	0.650	0.0806	$-2,596\ M_Y$
					$-2,840\ M_X$

Table 1. Average test conditions and trim targets; sign conventions: α_c + aft shaft tilt, M_Y + nose up, M_X + right side down.

The CFD/CSD simulations used these average conditions, and assume that each blade is identical in terms of mass distribution, structural properties, and trim-tab settings. Each rotor blade in the test is actually different, in ways both known (trim-tab setting) and unknown. As will be seen, measurements show that each blade exhibits different root motions and deflections. Note that some of the experimental data presented in this paper have been updated since the initial publication in References 6, 10. Generally speaking the corrections have been small. In the measured data presented here, rev-to-rev variations, when available, are shown with error bars.

Performance and Rotor Trim

A hierarchy of data is available from the NFAC tests. Performance data reflects integrated values over the entire rotor, and therefore comparison between computed and measured performance data can give an overall assessment of the fidelity of the simulation to the test. Details are masked by the integrated values however. Table 2 shows the comparison between computation and measurement for the (solidity-weighted) thrust, power, and propulsive force coefficients for the two test conditions.

		R42P60	R53P20
C_T/σ	(NFAC)	0.1002	0.0806
C_T/σ	(CFD)	0.1005	0.0809
%Diff.		0.3	0.4
C_P/σ	(NFAC)	0.00382	0.00845
C_P/σ	(CFD)	0.00376	0.00827
%Diff.		-1.6	-2.1
C_X/σ	(NFAC)	-0.00218	0.00956
C_X/σ	(CFD)	-0.00217	0.01008
%Diff.		-0.5	5.5

Table 2. Measured vs. computed performance data.

The computed power coefficient matches the experimental values to within 1.6 and 2.1 percent for R42P60 and R53P20, respectively. The propulsive coefficients match to within 0.5 and 5.5 percent for R42P60 and R53P20, respectively. The thrust computed from the CFD solver is within 0.4 percent of the measured value for both cases. Note that the target thrust (the measured value) is matched essentially exactly within the comprehensive code. The small differences in the CFD-computed thrust are a measure of losses encountered in a non-conservative load transfer process that only transfers three (normal force, chord force, and pitching moment) of the six force and moment components.

The trimming process employed here adjusts the collective and cyclic pitch components to meet thrust and moment targets. The final values from the trim process, extracted from CAMRAD-II output, are shown in Table 3. The root pitch angle, exclusive of built-in twist and elastic deformation, is described by $\theta = \theta_c + \theta_{1s}sin(\psi) + \theta_{1c}cos(\psi)(+higher\ hamonics)$. The collective angles (θ_c) in both simulations are slightly larger than the NFAC values, by 1.12° for R42P60 and by 0.62° for R53P20.

Sectional Airloads

As mentioned earlier, a number of pressure transducers became nonoperational or unreliable during the course of the

		R42P60	R53P20
θ_0	(NFAC)	7.88	13.07
θ_0	(CFD)	9.00	13.69
θ_{1s}	(NFAC)	−6.16	−9.06
θ_{1s}	(CFD)	−5.83	−8.47
θ_{1c}	(NFAC)	0.41	1.28
θ_{1c}	(CFD)	0.78	1.00

Table 3. Measured vs. computed control angles.

NFAC testing. For Runs 42 and 53, there was not a sufficient number of operational pressure transducers to provide sectional airloads for station $r/R = 0.550$. Also, for Run 53 the airloads stations at $r/R = 0.675$, 0.775, and 0.965 had a small number (7–8) of operational transducers on the lower surface of the blade. Outboard sectional airloads are generally of greater interest owing to higher loading and nonlinear phenomenon such as shock wave interactions. Because the aforementioned stations from Run 53 do not have sufficient transducers to provide viable sectional airloads, a common set of outboard stations, $r/R = 0.865$, 0.920 and 0.990 are examined for both test conditions, together with the station closest to the blade root, $r/R = 0.225$.

The NFAC sectional airloads data is derived solely from pressure integration, using a maximum of 30 (and often fewer) chordwise transducer locations at each station. In CFD simulations, sectional airloads are usually integrated over all points on the CFD surface at the radial location in question, and the integration includes both pressure and skin friction contributions. In Reference 16, CFD sectional airloads were obtained by integrating only the pressure contribution at locations corresponding to the transducer locations, and only at those locations where the transducer was deemed reliable. This pressure transducer status information is provided as part of the experimental data file for each test point. The same second-order, mapped-coordinate integration scheme used with the NFAC pressures was used with the CFD pressures. As a result, sectional airloads can be defined consistently in both CFD and experiment. Generally speaking this consistent integration leads to greatly improved correlation in chord force. The same process described in Reference 16 is followed in this paper for the computed sectional airloads.

The measured sectional airloads data shown here reflect a correction applied after the initial data release. The preliminary data used absolute pressures in the integration routine rather than relative $(P - P_{static})$ pressures that were expected by the routine. The resulting corrections were generally small, and principally affect the pitching moment. The CFD airloads were processed using the relative pressures, and so are consistent with the corrected NFAC data. The measured sectional airloads data are plotted with error bars denoting rev-to-rev variations. However, for these test conditions, the error bars are almost always smaller than the symbol size used in the plots.

Figure 5 shows the comparison of sectional airloads between CFD and NFAC data at radial stations $r/R = 0.225$, $r/R = 0.865$, $r/R = 0.920$ and $r/R = 0.990$ for the test condition R42P60. Figure 6 shows the corresponding data for R53P20. Ordinate ranges for each quantity (M^2C_n, M^2C_m, and M^2C_c) are held fixed between both test conditions and at all three stations, to allow direct comparison of relative magnitudes.

The general level of agreement between computation and measurement is favorable. At all four stations, the overall level of computed normal force, and the variation with azimuth, closely follows the measured normal force. The pitching moment is also well captured by the simulations, with the exception of $r/R = 0.865$, where the computation misses the magnitude of the nose-down pitching moment on the advancing side. Computed chord force, which often exhibits very large differences between computation and measurement, follows the trend of the measured data quite well, though there is a persistent offset from the measured values. As shown in Reference 16, this level of agreement in chord force is a direct result of the consistent integration of pressures between CFD and experiment.

The high advance ratio case, R53P20, exhibits a pronounced shock interaction on the advancing side in the outboard region of the blade. As the blade rotates through the advancing side, the upper surface, normally the suction surface, and the lower surface change roles, leading to the negative loading (negative M^2C_n) seen in (approximate) azimuth range of 90° to 150° at each of the three outboard stations. As the shock wave moves from the upper to the lower surface, a sharp change in pitching moment is evident near $\psi = 75°$.

Overall the level of agreement between simulation and measurement suggests that the aerodynamics are generally well captured at the outboard blade stations. This is reassuring, since deflections of the outer part of the blade will depend in large part on the aerodynamic loads. Before considering the elastic blade deflections, we will examine the blade root motions, as these form the basis for defining "rigid blade" motions, from which elastic deformations are measured.

Blade Root Motion

In this section, the computed blade root motions are extracted from sectional geometric data output by FUN3D at each time step during a rotorcraft simulation. This geometric data includes absolute pitch angle and quarter-chord location in both normal and chordwise directions in the blade reference frame. The blade reference frame is the coordinate frame used to define the unloaded, undeformed blade geometry. This data, in conjunction with other geometric data such as built-in blade twist, undeformed blade quarter-chord locations, and hinge offsets, allows the computed blade motions and deflections to be determined. The same type of motion extraction is possible not only at the root but at any other radial location at which the sectional geometric data is output. FUN3D uses this sectional geometric data internally to resolve the sectional airloads into normal and chordwise components (as shown in Figure 6 for example). Thus the computed blade motion data presented

here is obtained in a consistent way with the sectional airloads.

Comparisons of computed root pitch, root bending and root lag motions for R42P60 are shown in Figure 7. Comparison is made against all three measurement systems. Clearly, the measured root motion is different for each blade. In general the measured pitch angles for each blade are within approximately 1° of each other, the measured flap angles are within approximately 2.5° of each other, and the lag angles within approximately 1° to 2.5° of each other.

The root pitch angle shown in Figure 7 is exclusive of the built-in blade twist. The computed root pitch agrees very well with the laser data, however the laser data is slightly different from the crab-arm and BD pitch data. As observed when discussing the trimmed control angles, the computed mean pitch angle is roughly 1° higher than that measured by the crab-arm and BD systems.

The computed root flap angle generally falls within the bounds of blade-to-blade variation as measured by the crab-arm and laser systems. For the root flap angle, the crab-arm and laser data are closer to each other than to the BD data, but all three systems show similar flap motion.

The computed lag angles presented here have been increased by +7°. As discussed in Reference 28 regarding the flight-test program, during data acquisition, when the rotor hub is at 0° azimuth, the lag angle is +7°. The NFAC tests use the same azimuthal reference for data acquisition as the flight-test program. In the CFD model, however, the lag angle is 0° at the 0° azimuth reference point, thus necessitating the +7° increment to lag angle to allow direct comparison with the measured value.

While the predicted pitch and flap angles at the root compare reasonably well with the measured data, the predicted lag angle shows a more significant offset from the data, even accounting for the previously-mentioned +7° offset. The waveform of the lag response is reasonably well captured by the computation, but a +2° to +3° offset is observed between computation and measurement, with the largest difference being relative to the BD data. This residual lag offset has also been observed in References 10, 11. The variation in mean lag offset with rotor torque was examined in Reference 11 as a means of understanding the nature of the offset. There it was concluded that one or more of the physical properties of the model blade were likely inaccurate, and that errors in torque offset, chordwise center of gravity, or tension center were the most likely causes leading to the mean lag offset.

Figure 8 shows the same comparisons of computed and measured root motion for the R53P20 (high advance ratio) condition. Once again the pitch angle measured by the laser system is in best agreement with the computation, though the crab-arm and BD data agree better with each other than with the laser data.

Although the excursions in flap angle around the rotor disk are larger for R53P20 compared to R42P60, the mean flap angle is smaller (3.56° vs. 4.52°), which is consistent with the lower thrust level of R53P20. Once again the computed flap angles generally lie within the bounds of the blade-to-blade variation of the crab-arm and BD measurement, except in the range $\psi = 300°$ to $\psi = 360°$. For this case the laser measurements of flap angle are quite different than the crab-arm and BD measurements.

Compared to R42P60, the difference in mean lag angle between computation and measurement is smaller, particularly compared to the crab-arm and BD data. In fact the computed root lag angle follows the variation of the BD data quite closely, and with the computed lag nearly matching the BD data for blade 4. However, the BD data for lag is suspect. (Ref. 11)

Blade Deflections

For both computation and experiment, the evaluation of elastic blade deformations at a particular azimuth results from the subtraction, in the blade reference frame, of a hypothetically rigid blade from the instantaneous blade shape. These operations are only performed along the blade quarter chord line, so that strictly speaking, the "blade deformations" are "deformations of the quarter chord". The instantaneous orientation of the hypothetically rigid blade is determined from the instantaneous root pitch, flap, and lag angles discussed in the preceding section. Note that because the determination of elastic deformations depends on the root motions, errors in the root motions will propagate into errors in the elastic deformation. This is true for both computation and measurement.

Consider a plane orthogonal to the axis of rotation, and centered on the rotor hub. Flap is a vertical motion out of this plane, and lag a motion in this plane. Wherever the blade quarter chord differs from the feathering axis, changes in root pitch lead to out-of-plane (flap) motion of the hypothetical rigid quarter chord in the tip region. On the swept-tip portion of the UH-60A blade, this out-of-plane motion due to pitch increases linearly with radius, following the increasing displacement of the quarter-chord line from the feathering axis. This out of plane tip motion is accounted for in the hypothetical rigid blade.

The elastic component of the flapping motion is referred to as elastic bending, while the elastic component of lag motion is referred to as chordwise or in-plane bending. Chordwise bending is much smaller in magnitude than elastic bending. Whether or not sufficiently accurate measurements of the chordwise bending by using the BD system are possible is still subject to some debate. No in-plane bending comparisons are shown here.

Figure 9 shows the comparison of predicted and measured elastic bending and twist at $r/R = 0.97$ (just inboard of the tip) for the R42P60 conditions. Overall, the elastic bending shows very good agreement between the computed data and BD data. A phase difference of roughly 20° is observed, but otherwise both the amplitude and waveform of the elastic bending are very well captured in the computation. The blade-to-blade scatter is on the order of 2.5 inches. If the deformed shape of

a blade (but not the orientation) was known exactly, an uncertainty in the root flap angle of 0.5° would lead to a scatter in elastic bending of 2.8 inches at the tip of the 322 inch radius rotor.

While the waveform of the elastic twist at $r/R = 0.97$ is reasonably well captured in the simulation, the mean elastic twist is more negative, i.e., shows increased washout, compared to the BD data. This is not too surprising since the mean root pitch angle was observed to be greater in the simulation than was measured. Since the measured thrust is matched to a close approximation by the trim process, a decrease in thrust in the outboard sections due to greater washout would need to be compensated by an increase in the thrust due to higher inboard pitch.

Figure 10 shows the comparison of predicted and measured elastic bending and twist at $r/R = 0.97$ for the R53P20 conditions. The same level of agreement between computation and measurement is obtained as for the the R42P60 conditions. The mean tip washout is greater for the higher advance ratio conditions, but the offset of the mean washout between computation and measurement is roughly the same as for R42P60.

Finally, radial variations in elastic bending and twist are compared. Three azimuthal locations are examined: $\psi = 0°$, $\psi = 150°$, and $\psi = 255°$. The last two correspond, to the (approximate) azimuthal location where the most negative (downward) elastic tip bending occurs, and where the most positive (upward) tip bending occurs, respectively.

Figures 11 and 12 show a comparison of radial variation in elastic bending and twist for the R42P60 and R53P20 test conditions, respectively. The computed elastic bending is in reasonably good agreement with the measured bending for both test conditions. As would be expected, the radial variation of elastic bending primarily consists of a first beam bending mode, although higher bending modes are clearly present.

The correlation between computation and measurement of elastic twist as a function of radius is considerably less favorable than that for elastic bending, particularly at $\psi = 150°$. As seen in Figures 7 and 8, $\psi = 150°$ is in the region where the difference in root pitch between computation and BD data is the largest. The elastic twist data at $\psi = 0°$ for blade 1 under the R42P60 condition certainly seems suspect because the values actually increase toward the root. The radial distributions show that the differences in tip elastic twist seen in Figure 9, are not just localized to the tip, but are present across the entire blade.

As mentioned earlier, errors in the rigid motions at the root will propagate into errors in the elastic deflections. Although not carried out here, estimated corrections can be applied to computed deflections by modifying the hypothetical rigid blade notion with offsets arising from the differences between measured and computed rigid root motions, as done in Reference 11.

CONCLUDING REMARKS

The wide range of data being made available from the full-scale tests of a UH-60A rotor in the NFAC are proving to be extremely valuable in evaluating computational models. The range of data available, from global measures such a rotor power and propulsive force, to finer-grain measures such as sectional airloads and blade deflections, down to the level of unsteady pressures, provides a useful hierarchy for computational validation.

In this paper we explored several levels of this data hierarchy, with emphasis placed on correlation of computed and measured blade displacements. Both rigid motion at the root and elastic deflections along the blade were examined. Two test conditions were modeled, one a moderate thrust, moderate advance ratio case with nulled pitch and roll moments, and a second representative of 1-g level flight at a high advance ratio.

In terms of overall performance measures, the measured power coefficients for the high advance ratio case were computed to within approximately two percent, and the computed propulsive force to within approximately five percent. For the moderate advance ratio case the computed results for propulsive power were considerably better.

Sectional airloads were extracted from the computation in a manner consistent with the tunnel measurements, using only the pressure contribution, and only at locations corresponding to operational pressure transducers. The correlation between computation and measurement was generally very good.

Blade root motions were compared with data from three independent measurement systems, one of which, the photogrammetry-based blade displacement system, was used to obtain displacements along the blades as well as at the root. The cases chosen for this paper were ones for which BD data were taken for each of the four blades over the entire rotor disk. Considerable blade-to-blade variation in the measured data is observed, particularly in flap and lag. Typically the data from the crab-arm and BD systems agreed with each other better than the laser system. Root pitch and flap were reasonably captured by the simulations, though – and this is most readily apparent for the higher advance ratio – there is a phase shift of approximately 20° between the BD data and computed results for both pitch and flap. The cause of this shift is not yet understood.

Elastic bending and twist are determined by subtracting from the instantaneous blade shape a hypothetically rigid blade that moves with the blade-root motion. At the tip, where elastic deformations are largest, the elastic bending predicted by the computation is in excellent agreement with the data, apart from the 20° shift also seen in the root motion. Elastic twist on the other hand, is consistently underpredicted in the simulations.

Because the elastic motions are derived motions relying on the accuracy of the root motion, future work perhaps should examine the absolute position and orientation of the blade,

rather than introduce the artifice of the elastic deflections relative to a hypothetically rigid blade.

ACKNOWLEDGEMENTS

The authors would like to thank the entire Airloads Wind Tunnel Test team for collecting, processing and making available the data from the NFAC test. The authors would especially like to thank Mr. Thomas Norman of NASA Ames Research Center for many helpful discussions regarding the NFAC data and for providing the updated sectional airloads, crab-arm, and laser system blade root data. The authors would also like to thank Mr. Danny Barrows of NASA Langley Research Center and Mr. Alpheus Burner of Jacobs Technology for providing the most recent blade displacement data.

REFERENCES

[1]Kufeld, R. M., Balough, D. L., Cross, J. L., Studebaker, K. F., Jennison, C. D., and Bousman, W. G., "Flight Testing of the UH-60A Airloads Aircraft," *American Helicopter Society 50th Annual Forum Proceedings*, 1994.

[2]Bousman, W. G. and Kufeld, R. M., "UH-60A Airloads Catalog," NASA TM 2005-212827, Aug. 2005.

[3]Biedron, R. and Lee-Rausch, E., "Computation of UH-60A Airloads Using CFD/CSD Coupling On Unstructured Meshes," *American Helicopter Society 67th Annual Forum Proceedings*, 2011.

[4]Sankaran, V., Potsdam, M., Wissink, A., Datta, A., Jayaraman, B., and Sitaraman, J., "Rotor Loads Prediction in Level and Maneuvering Flight Using Unstructured-Adaptive Cartesian CFD," *American Helicopter Society 67th Annual Forum Proceedings*, 2011.

[5]Chaderjian, N. M. and Ahmad, J. U., "Detached Eddy Simulation of the UH-60 Rotor Wake Using Adaptive Mesh Refinement," *American Helicopter Society 68th Annual Forum Proceedings*, 2012.

[6]Norman, T., Peterson, R., Shinoda, P., and Datta, A., "Full-Scale Wind Tunnel Test of the UH-60A Airloads Rotor," *American Helicopter Society 67th Annual Forum Proceedings*, 2011.

[7]Romander, E., Norman, T., and Chang, I.-C., "Correlating CFD Simulations with Wind Tunnel Test for the Full-Scale UH-60A Airloads Rotor," *American Helicopter Society 67th Annual Forum Proceedings*, 2011.

[8]Marpu, R. P., Sankar, L. N., Norman, T. R., Egold, T. A., and Makinen, S., "Analysis of the UH-60A Rotor Loads Using Wind Tunnel Data," AIAA Paper 2013-0635, Jan. 2013.

[9]Ahmad, J. U., Yamauchi, G. K., and Kao, D. L., "Comparison of Computed and Measured Vortex Evolution for a UH-60A Rotor in Forward Flight," AIAA Paper 2013-3160, June 2013.

[10]Abrego, A. I., Olson, L. E., Romander, E. A., Barrow, D. A., and Burner, A. W., "Blade Displacement Measurement Technique Applied to a Full-Scale Rotor Test," *American Helicopter Society 68th Annual Forum Proceedings*, 2012.

[11]Romander, E., Meyn, L., Norman, T. R., Barrows, D., and Burner, A., "Blade Motion Correlation For The Full-Scale UH-60A Airloads Rotor," *Fifth Decennial AHS Aeromechanics Specialists Conference*, Jan. 2014.

[12]Lee-Rausch, E. M. and Biedron, R. T., "FUN3D Airload Predictions for the Full-Scale UH-60A Airloads Rotor in a Wind Tunnel," *American Helicopter Society 69th Annual Forum Proceedings*, 2013.

[13]Yeo, H. and Romander, E., "Loads Correlation of a Full-Scale UH-60A Airloads Rotor in a Wind Tunnel," *Journal of the American Helicopter Society*, Vol. 58, No. 2, April 2013, pp. 1–18.

[14]Chang, I.-C., , Norman, T., and Romander, E., "Airloads Correlation of the UH-60A Rotor Inside the 40- by 80-Foot Wind Tunnel," AIAA Paper 2013-0636, Jan. 2013.

[15]Floros, M. W., Singh, R., and Kang, H., "Effects of the Fuselage and Tunnel Walls on Correlation of CFD/CSD Computations and Test Data," *American Helicopter Society 69th Annual Forum*, May 2013.

[16]Biedron, R. T. and Lee-Rausch, E. M., "An Examination of Unsteady Airloads on a UH-60A Rotor: Computation versus Measurement," *American Helicopter Society 68th Annual Forum Proceedings*, 2012.

[17]Barrows, D. A., Burner, A. W., Abrego, A. I., and Olson, L. E., "Blade Displacement Measurements of the Full-Scale UH-60A Airloads Rotor," AIAA Paper 2011-3655, June 2011.

[18]Biedron, R. T., Derlaga, J. M., Gnoffo, P. A., Hammond, D. P., Jones, W. T., Kleb, B., Lee-Rausch, E. M., Nielsen, E. J., Park, M. A., Rumsey, C. L., Thomas, J. L., and Wood, W. A., "FUN3D Manual: Version 12.4-69883," NASA TM 2014-218179, March 2014.

[19]Noack, R. W., "DiRTlib: A Library to Add an Overset Capability to Your Flow Solver," AIAA Paper 2005-5116, June 2005.

[20]Noack, R. W., Boger, D. A., Kunz, R. F., and Carrica, P. M., "SUGGAR++: An Improved General Overset Grid Assembly Capability," AIAA Paper 2009-3992, June 2009.

[21]Spalart, P. R. and Allmaras, S. R., "A One-Equation Turbulence Model for Aerodynamic Flows," *La Recherche Aerospatiale,* No. 1, 1994, pp. 5–21.

[22]Roe, P. L., "Approximate Riemann Solvers, Parameter Vectors, and Difference Schemes," *Journal of Computational Physics*, Vol. 43, 1981, pp. 357–372.

[23]Vatsa, V. N. and Carpenter, M. H., "Higher-Order Temporal Schemes with Error Controllers for Unsteady Navier-Stokes Equations," AIAA Paper 2005-5245, June 2005.

[24]Vatsa, V. N., Carpenter, M. H., and Lockard, D. P., "Re-evaluation of an Optimized Second Order Backward Difference (BDF2OPT) Scheme for Unsteady Flow Applications," AIAA Paper 2010-0122, Jan. 2010.

[25]Biedron, R. T. and Thomas, J. L., "Recent Enhancements To The FUN3D Flow Solver for Moving Mesh Applications," AIAA Paper 2009-1360, Jan. 2009.

[26]Johnson, W., "Rotorcraft Aerodynamics Models for a Comprehensive Analysis," *American Helicopter Society 54th Annual Forum Proceedings*, 1998.

[27]Yeo, H., Bousman, W, G., and Johnson, W., "Performance Analysis of a Utility Helicopter with Standard and Advanced Rotor," *Journal of the American Helicopter Society*, Vol. 49, No. 3, July 2004, pp. 250–270.

[28]Kufeld, R. M. and Bousman, W. G., "Technical Note: UH-60A Airloads Program Azimuth Reference Correction," *Journal of the American Helicopter Society*, Vol. 50, No. 2, 2005, pp. 211–213.

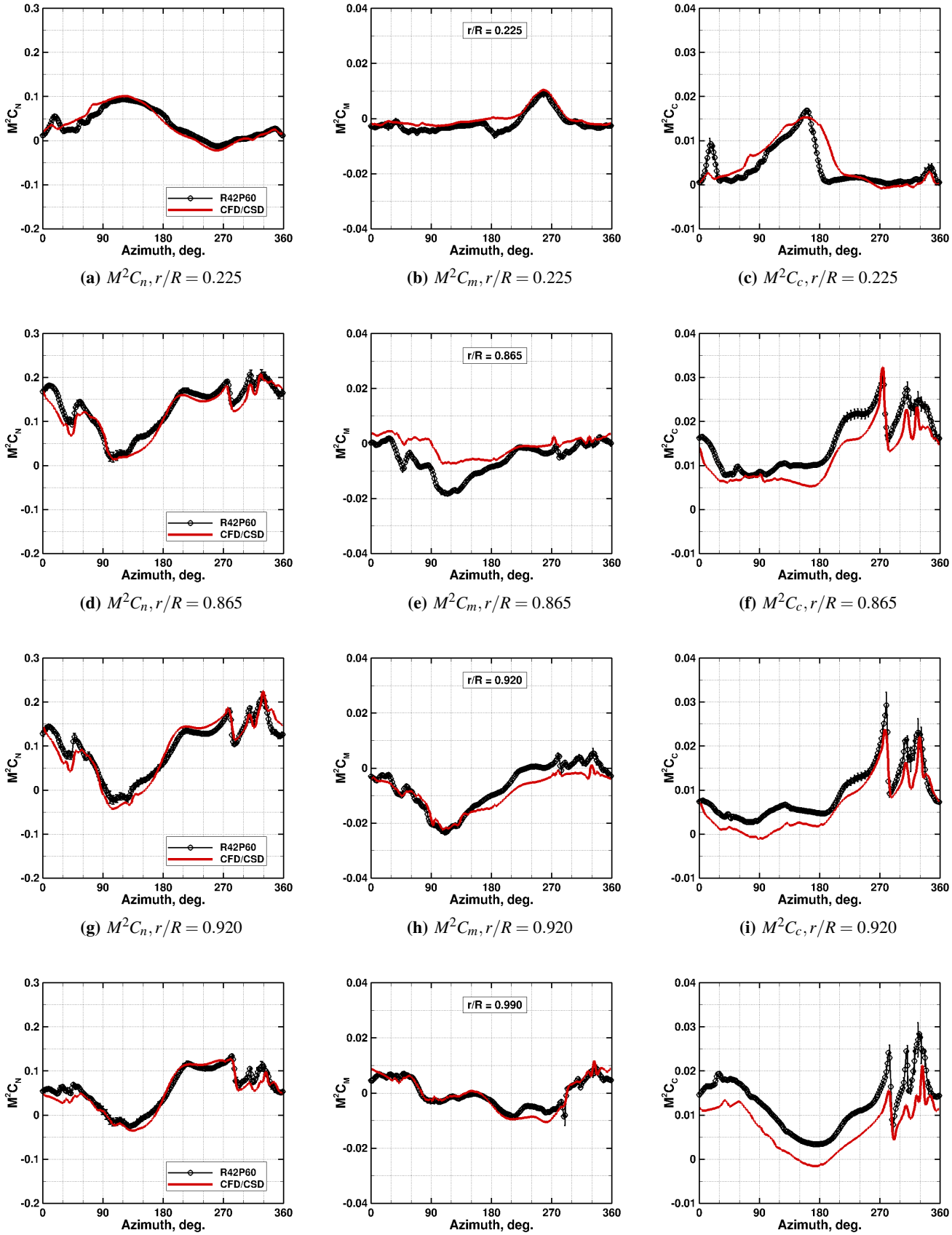

(a) $M^2C_n, r/R = 0.225$ **(b)** $M^2C_m, r/R = 0.225$ **(c)** $M^2C_c, r/R = 0.225$

(d) $M^2C_n, r/R = 0.865$ **(e)** $M^2C_m, r/R = 0.865$ **(f)** $M^2C_c, r/R = 0.865$

(g) $M^2C_n, r/R = 0.920$ **(h)** $M^2C_m, r/R = 0.920$ **(i)** $M^2C_c, r/R = 0.920$

(j) $M^2C_n, r/R = 0.990$ **(k)** $M^2C_m, r/R = 0.990$ **(l)** $M^2C_c, r/R = 0.990$

Fig. 5. Comparison of sectional forces and pitching moments at $\mathbf{r/R = 0.865, r/R = 0.920,}$ and $\mathbf{r/R = 0.990}$ for R42P60 ($\mu = \mathbf{0.300}, \mathbf{C_T/\sigma = 0.1002}, \alpha_c = \mathbf{0.78}^\circ$).

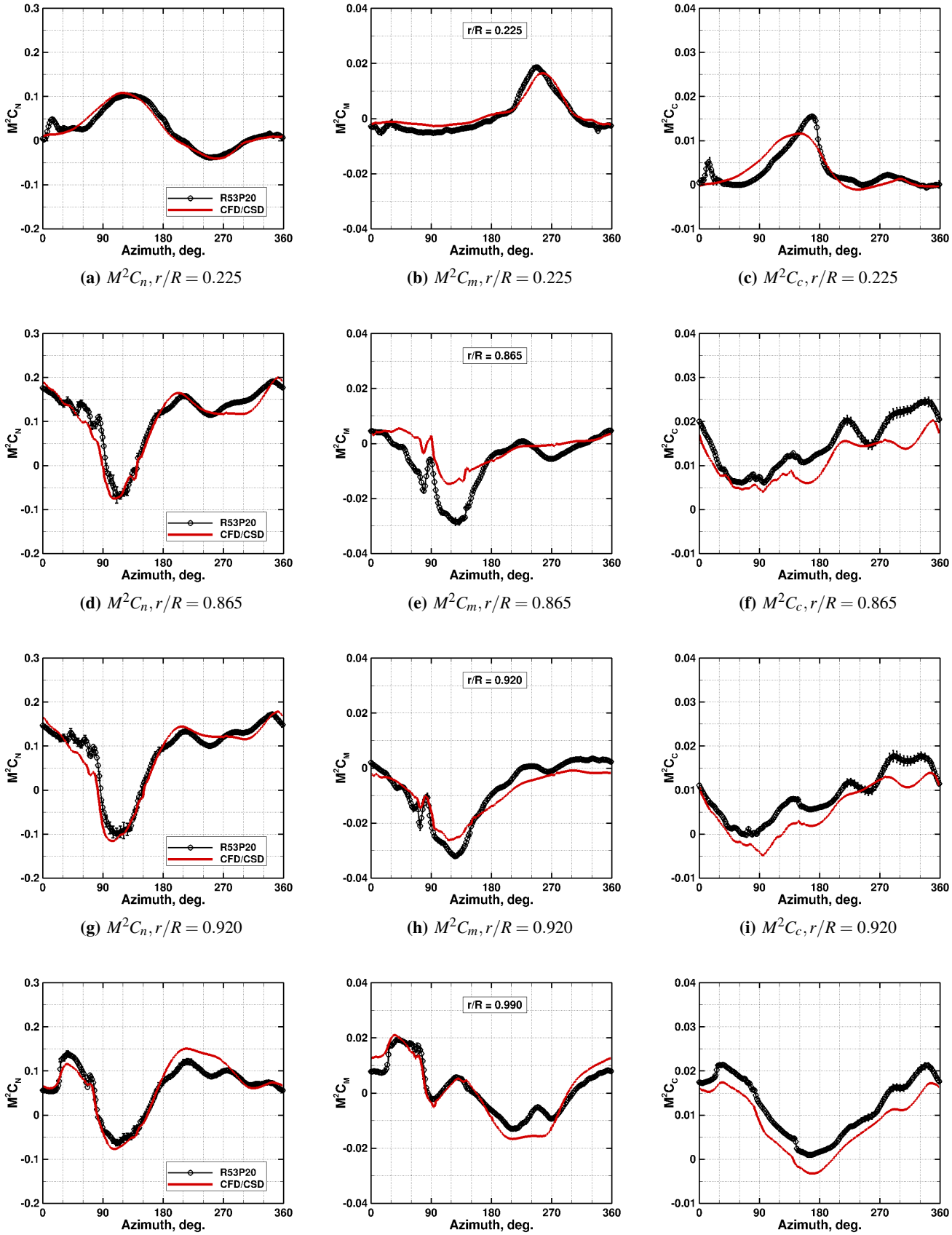

(a) $M^2C_n, r/R = 0.225$ **(b)** $M^2C_m, r/R = 0.225$ **(c)** $M^2C_c, r/R = 0.225$

(d) $M^2C_n, r/R = 0.865$ **(e)** $M^2C_m, r/R = 0.865$ **(f)** $M^2C_c, r/R = 0.865$

(g) $M^2C_n, r/R = 0.920$ **(h)** $M^2C_m, r/R = 0.920$ **(i)** $M^2C_c, r/R = 0.920$

(j) $M^2C_n, r/R = 0.990$ **(k)** $M^2C_m, r/R = 0.990$ **(l)** $M^2C_c, r/R = 0.990$

Fig. 6. Comparison of sectional forces and pitching moments at $\mathbf{r/R = 0.865, r/R = 0.920,}$ and $\mathbf{r/R = 0.990}$ for R53P20 ($\mu = 0.371, C_T/\sigma = 0.0806, \alpha_c = -7.99^\circ$).

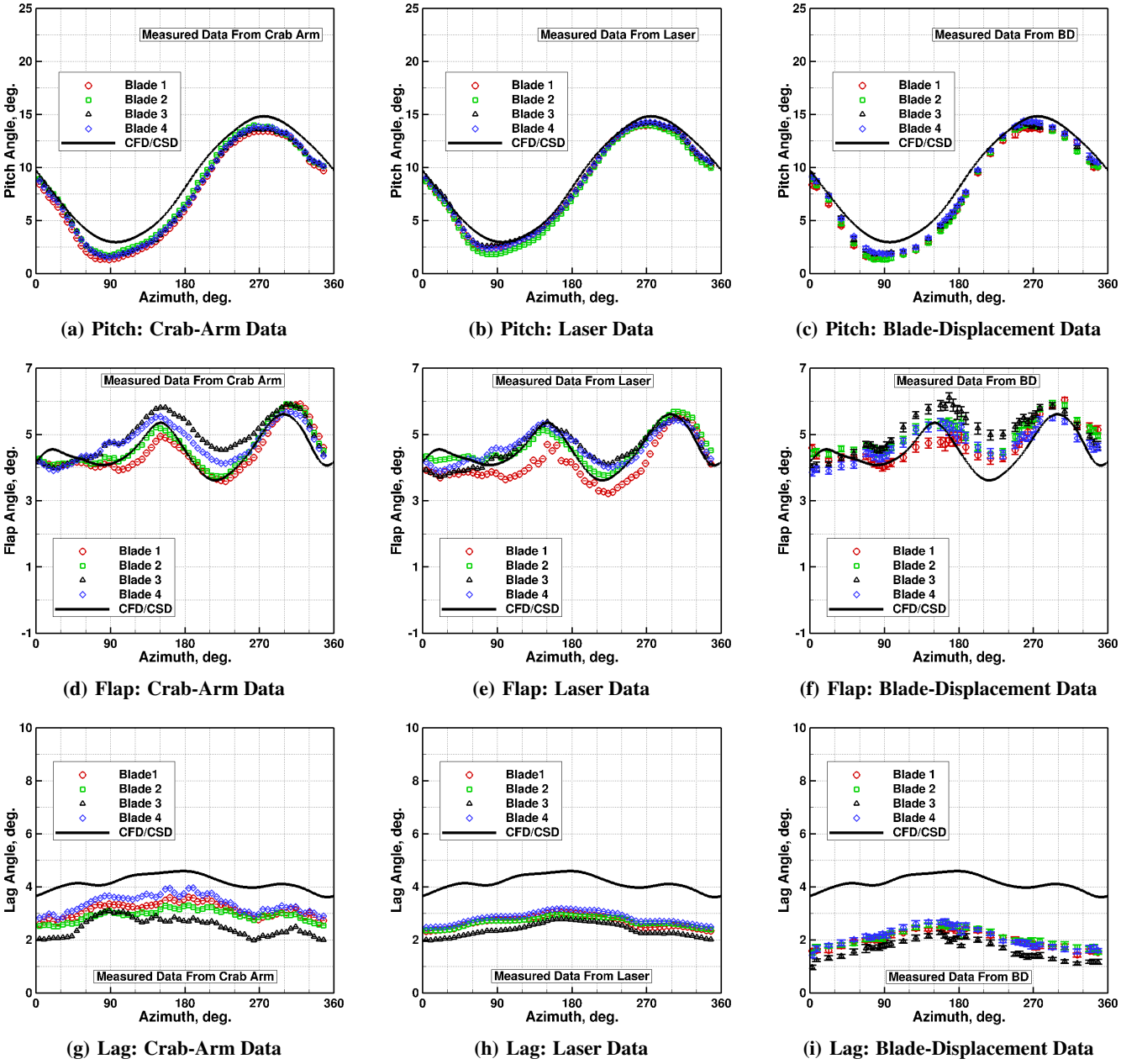

(a) Pitch: Crab-Arm Data (b) Pitch: Laser Data (c) Pitch: Blade-Displacement Data

(d) Flap: Crab-Arm Data (e) Flap: Laser Data (f) Flap: Blade-Displacement Data

(g) Lag: Crab-Arm Data (h) Lag: Laser Data (i) Lag: Blade-Displacement Data

Fig. 7. Comparison of predicted and measured blade root motion, R42P60 ($\mu = 0.300, C_T/\sigma = 0.1002, \alpha_c = 0.78^\circ$).

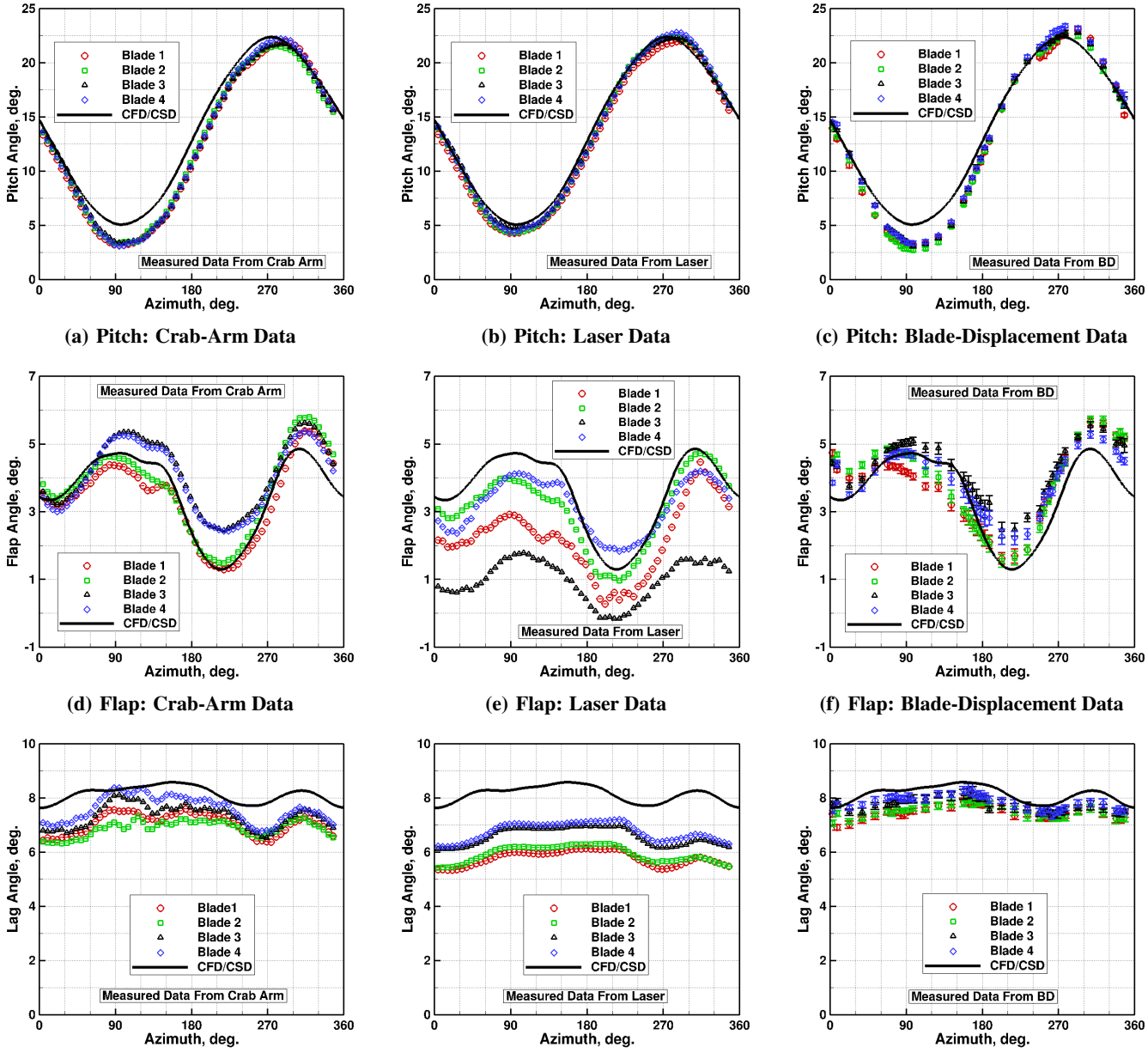

(a) Pitch: Crab-Arm Data (b) Pitch: Laser Data (c) Pitch: Blade-Displacement Data

(d) Flap: Crab-Arm Data (e) Flap: Laser Data (f) Flap: Blade-Displacement Data

(g) Lag: Crab-Arm Data (h) Lag: Laser Data (i) Lag: Blade-Displacement Data

Fig. 8. Comparison of predicted and measured blade root motion, R53P20 ($\mu = 0.371, C_T/\sigma = 0.0806, \alpha_c = -7.99^\circ$).

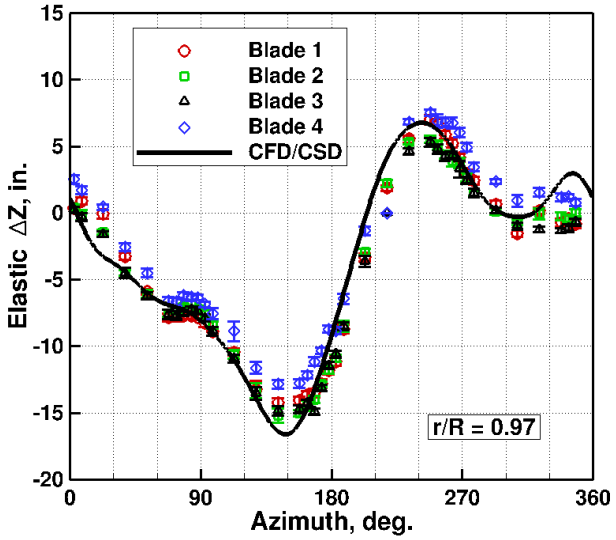

(a) Elastic Bending

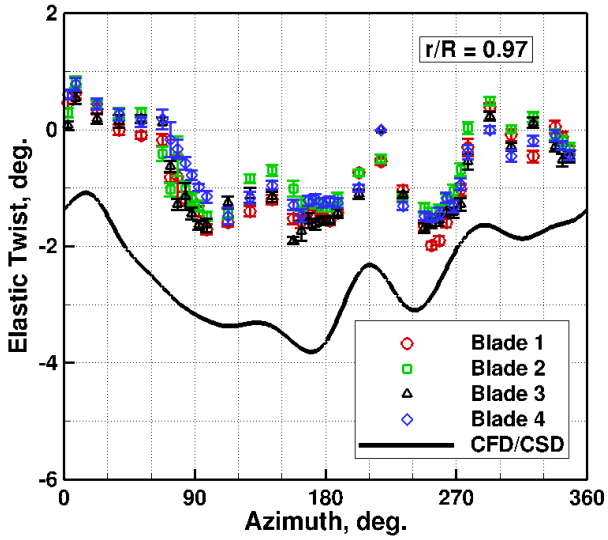

(b) Elastic Twist

Fig. 9. Comparison of predicted and measured elastic bending and twist at $r/R = 0.97$, R42P60 ($\mu = 0.300, C_T/\sigma = 0.1002, \alpha_c = 0.78^\circ$).

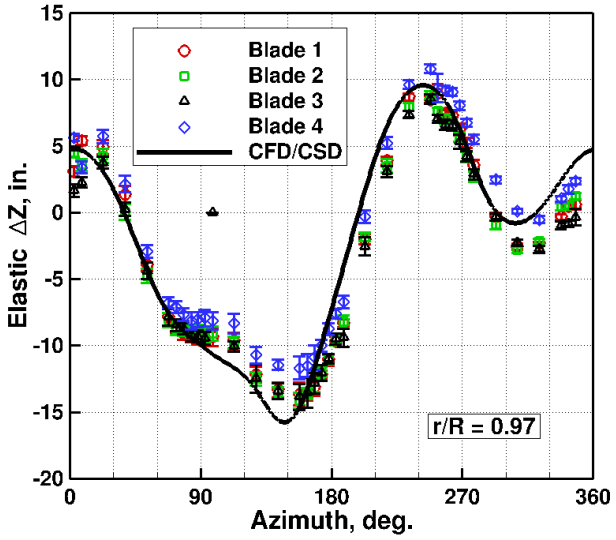

(a) Elastic Bending

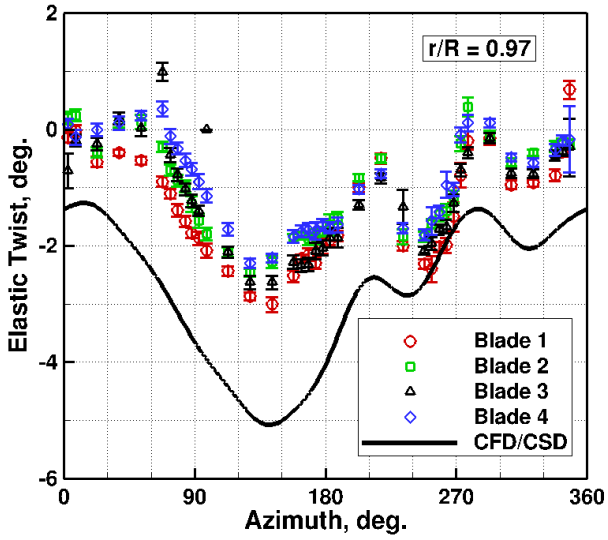

(b) Elastic Twist

Fig. 10. Comparison of predicted and measured elastic bending and elastic twist at $r/R = 0.97$, R53P20 ($\mu = 0.371, C_T/\sigma = 0.0806, \alpha_c = -7.99^\circ$).

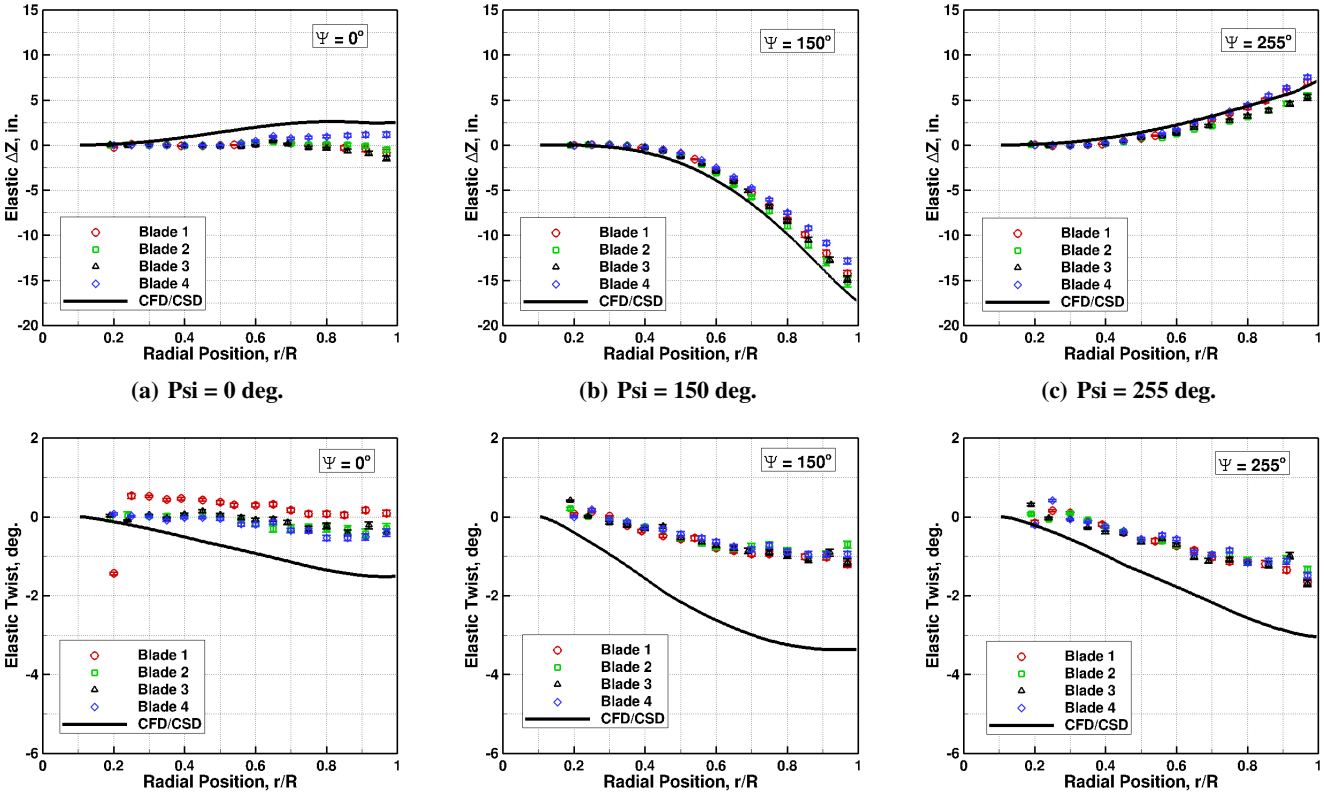

(a) Psi = 0 deg. (b) Psi = 150 deg. (c) Psi = 255 deg.

(d) Psi = 0 deg. (e) Psi = 150 deg. (f) Psi = 255 deg.

Fig. 11. Comparison of radial variation in elastic bending and elastic twist at selected azimuthal locations, R42P60 ($\mu = 0.300, C_T/\sigma = 0.1002, \alpha_c = 0.78^\circ$).

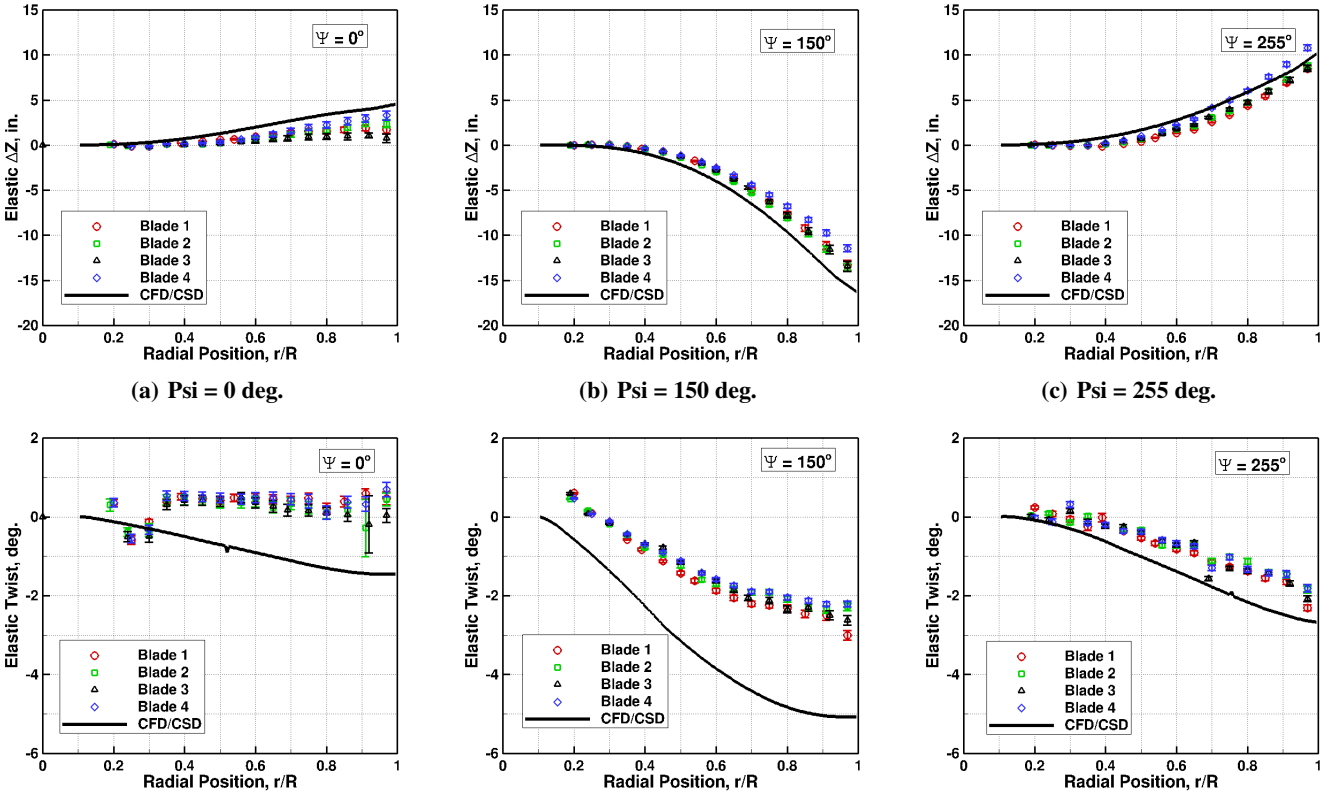

(a) Psi = 0 deg. (b) Psi = 150 deg. (c) Psi = 255 deg.

(d) Psi = 0 deg. (e) Psi = 150 deg. (f) Psi = 255 deg.

Fig. 12. Comparison of radial variation in elastic bending and twist at selected azimuthal locations, R53P20 ($\mu = 0.371, C_T/\sigma = 0.0806, \alpha_c = -7.99^\circ$).